ACS APPLIED ENERGY MATERIALS

www.acsaem.org Article

Potential Cycling of Silver Cathodes in an Alkaline CO_2 Flow Electrolyzer for Accelerated Stress Testing and Carbonate Inhibition

Emiliana R. Cofell, Zachary Park, Uzoma O. Nwabara, Lauren C. Harris, Saket S. Bhargava, Andrew A. Gewirth, and Paul J. A. Kenis*

Cite This: https://doi.org/10.1021/acsaem.2c01308 Read Online

ACCESS | Metrics & More | Article Recommendations | Supporting Information

ABSTRACT: The electrochemical reduction of CO_2 (CO_2RR) holds promise for the reduction of environmentally taxing CO_2 emissions, for the carbon-neutral production of valuable fuels and chemicals, and for storage of excess renewable energy from intermittent sources such as wind and solar in chemical products. Durability of cathodes used in high-throughput CO_2RR systems is of paramount importance for the commercial readiness of the CO_2RR technology. In this study, we investigate the durability of silver-coated gas diffusion electrode cathodes under potential cycling conditions to simulate the impact of repeated cycles of startup and shutdown as might be experienced in connection with a variable renewable power source. We determine that cycling can impact the cathode *via* two distinct degradation mechanisms: (1) carbonate formation at negative potentials and (2) catalyst layer restructuring and loss in the relatively positive "oxide formation" potential range. We also explore tailored potential cycling as a mechanism for inhibiting carbonate formation by interrupting the high concentration of OH^- at the catalyst layer. The findings from this work lend insight into the types of variable potential operating conditions under which CO_2RR systems can deliver continuous, robust performance.

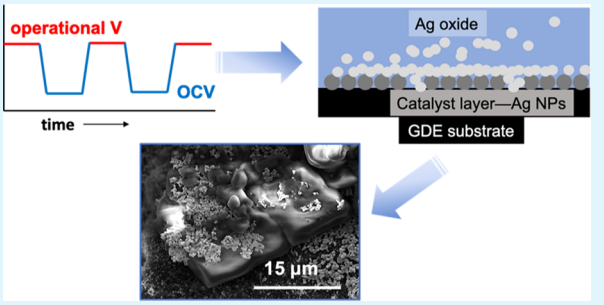

KEYWORDS: *electrochemical CO_2 reduction, durability, potential cycling, silver oxide, alkaline, GDE, degradation*

1. INTRODUCTION

Despite an increase in greenhouse gas emission-reduction policies and public concern about the ecological devastation caused by climate change, worldwide fossil fuel use continues to drive an increase in CO_2 emissions.[1] These emissions have resulted in rising temperatures and far-ranging negative impacts including severe weather events and declining crop yields.[1] To combat these consequences, CO_2 emissions need to be reduced across all sectors using a variety of established and emerging technologies.

A range of approaches are being explored to address CO_2 emissions and other greenhouse gasses at scale, including mineral carbonization, biological utilization, and chemical utilization including photochemical and electrochemical reduction.[2] One promising approach is the electrochemical reduction of carbon dioxide (CO_2RR) to value-added intermediates such as carbon monoxide (CO), ethanol, and ethylene that in turn can be used for the production of high-energy-density fuels and commodity chemicals.[3] CO_2RR coupled with renewable electricity from wind and solar sources provides a carbon neutral or carbon negative method for producing these valuable chemicals while recycling existing CO_2 emissions. Additionally, CO_2RR electrolyzers coupled with variable renewable energy sources represent an opportunity for electrochemical energy storage in the chemical bonds of products for excess power generated at peak production times.

Substantial prior work has reported on transition-metal catalysts that exhibit high activity and stability for CO_2RR to these various products.[4,5] For example, Au and Ag exhibit Faradaic efficiencies (FEs) ≥90% for CO production.[6] Currently, these catalysts are being tested for performance and durability in scalable electrode and cell configurations such as flow electrolyzer- and membrane electrode assembly (MEA)-based systems. Both use gas diffusion electrodes (GDEs) or GDE-like electrodes to achieve high product conversion rates.[7−9] High current density (activity), low overpotentials (high energy efficiency), high product FE (selectivity), and extensive durability/stability are all important metrics for determining industrial-scale viability.

To be implemented industrially, CO_2RR catalysts, electrodes, and systems must be able to sustain high activity and selectivities for extended periods of time, leading to an

Received: April 29, 2022
Accepted: September 2, 2022

emerging focus on electrode durability. Technoeconomic analyses of CO_2RR agree that an economically viable process would require at least 3000 h and up to 20,000 h of the stable performance.[10,11] Some GDE-based configurations have achieved hundreds of hours of operation, but systematic study of associated degradation mechanisms still is lacking.[12] Additionally, no prior study is available of how GDE stability is impacted by the application of variable potential or by repeated start-up and shutdown cycles. These variable conditions could result from a CO_2RR system being employed as an electrochemical energy storage method for excess wind and solar power, especially in a distributed electrical grid. One can envision CO_2RR electrolyzers used for electrochemical energy storage in a distributed grid relying on variable, renewable energy sources. Overproduction of energy by wind or solar sources can be mitigated by storage of excess energy in the bonds of chemicals and fuels produced *via* CO_2RR.[13] Studying the impact of varying operation potentials and startup/shutdown on these electrochemical systems will be key to widespread implementation of the CO_2RR electrolysis technology for energy storage and chemical manufacturing.

Accelerated stress testing (**AST**) is a method that has been used in other systems such as proton exchange membrane fuel cells (PEMFCs) and water electrolyzers to simulate these variable conditions.[14,15] For example, PEMFC systems have been operated in high-temperature and high relative humidity environments, as wells as under a variety of potential profiles and load cycling conditions to simulate the impact of potential variation during normal operation and during startup and shutdown on the fuel cell.

In this paper, we design **AST** methods to study the impact of potential cycling on the catalyst layer and GDE incorporated in an alkaline flow CO_2RR electrolyzer. We employ a variety of potential cycling **AST** protocols to simulate startup and operation interspersed with periods of shutdown and inactivity, varying the amplitude over a series of tests on a silver-coated GDE. We correlate degradation occurring *via* carbonate formation in high potential ranges, guided by results from our previous work.[16] Furthermore, we observed and studied catalyst layer restructuring due to silver oxide formation, as well as dissolution and loss of the catalyst in lower potential ranges. Performance loss from these degradation mechanisms occurs rapidly within the first hours of cycling and eventually halts CO_2RR to CO. Conversely, we observe that applying tailored potential cycles outside of the oxide formation range may have an inhibiting effect on carbonate deposit formation on the catalyst layer, a process that we will explain herein. Overall, we show **AST** studies presented here are elegant methods to elucidate long-term degradation mechanisms and its impact on the GDE performance over time, essential to the advance CO_2RR technology for energy storage and sustainable chemical manufacturing.

2. EXPERIMENTAL SECTION

2.1. Electrode Preparation. CO_2RR cathodes were prepared in batches of four by sonicating 10 mg of Ag nanopowder (Sigma Aldrich, <150 nm particle size, 99% trace metals basis)—a product which works very well for dispersion in an ink and airbrushing a uniform catalyst layer onto our GDE substrates—with 300 μL of deionized (DI) water, 26 μL of Nafion (5 wt % Fuel Cell Earth) binder, and 300 μL of isopropyl alcohol (IPA) for 20−30 min. This ink was airbrushed onto Sigracet 35 BC GDE (Fuel Cell Store) carbon paper substrate to obtain an Ag loading of 0.5 mg cm^{-2} (±10%) with the custom airbrushing setup described in previous work.[11] Next, the cathodes were cut into approximately 1 cm × 2.5 cm rectangles in order to fit into the flow cell. The area used in each reaction was held constant at 1 cm^2—both the gas flow chamber and electrolyte flow chamber measure 0.5 cm × 2 cm.

Anodes (for the oxygen evolution reactions, OER) were prepared in a similar manner, using Iridium(IV) oxide nanoparticles (Alfa Aesar, non-hydrate). The anode ink was prepared by mixing 80 mg of IrO_2 nanoparticles with 256 μL of Nafion binder and about 2400 mL each of DI water and IPA. The ink was airbrushed to obtain an IrO_2 loading of 4 mg cm^{-2} (±10%).

2.2. Electrochemical Cell. Experiments were carried out in custom electrochemical flow cells designed by our laboratory and manufactured by the machine shop at the University of Illinois at Urbana-Champaign, as reported in previous work.[16] The flow cell includes a stainless-steel gas flow cathode chamber, a Polyether ether ketone (PEEK) electrolyte flow chamber, and a stainless-steel anode chamber. For each experiment, the cell was assembled using a silicone gasket around the cathode to maintain an airtight environment for the cathode reaction, and manually clamped together. Polyethylene tubing (0.5 mm in diameter) was used for both gas and electrolyte flow. More information on cell assembly and design can be found in the Supporting Information.

2.3. Electrolysis Operation Conditions. An electrolyte flow rate of 1 mL/min was established using a peristaltic pump (Cole Parmer Masterflex L/S). CO_2 was flowed into the cell using a mass flow controller (Cole Parmer) at a rate of 17 sccm. An Ag/AgCl reference electrode (Basi RE-5B) fitted with a porous frit was connected to the electrolyte inlet tube. The active area of each electrode was 1 cm^2 during testing. For some tests, gas products were periodically collected every 15 cycles and analyzed using a gas chromatograph (Thermo Finnegan Trace GC) furnished with a thermal conductivity detector.

CO_2 electroreduction was carried out using 2 M KOH. The electrolyte was prepared using semiconductor grade ultra-pure (99.9%) KOH pellets purchased from Sigma-Aldrich. Potential cycles were applied, and current response was recorded using a potentiostat (Metrohm Autolab PGSTAT302N). We recorded cathode potential using digital multimeters (Crenova, MS8233D) and assessed the CO FE by using the Thermo Finnegan Trace GC to measure CO and CO_2 at half hour intervals; the FE was calculated according to the instrument calibration and ratio of CO and CO_2 peaks. More information about the FE calculation can be found in the Supporting Information. After completing each experiment, all cathodes were immediately and thoroughly rinsed with DI water for 10 s each and dried with nitrogen before being stored for characterization.

To simulate the impact of variable potential, in particular startup and shutdown cycles, on a CO_2RR electrolyzer, we applied trapezoidal potential waveforms of varying amplitudes. We chose a potential within the CO_2 reduction range as the "on" state and either 0 V or the measured open-circuit voltage (OCV) as the "off" state. In all cases expect when specifically noted, cell potential was controlled, and the results are presented in terms of the potential applied to the entire cell. All cathode potentials are compared with an Ag/AgCl reference electrode. **AST 1** consisted of a ramp from 0 to −3 V at 250 mV/s, a 55 s hold at −3 V, a ramp from −3 to 0 V, and a 55 s hold at 0 V. Thus, in total, each cycle took 2 min, 14 s. The scan rate used in all subsequent tests was also 250 mV/s, and the duration of each cycle and the total testing time varied accordingly. **AST 2** maintained the same parameters but cycled from 0 to −2 V. To simulate a more realistic "off" state for the system, we then repeated both tests cycling to the system's OCV instead of 0 V. The OCV was measured every 15 cycles to adjust for changing conditions throughout the test. **AST 3** cycled from −3 V to OVC, and **AST 4** cycled from −2 V to OCV. Each of these four tests consisted of 90 cycles, for a total testing duration of around 3 h. For **AST 5**, the cell potential was cycled from −1.75 to −3 V at a scan rate of 250 mV/s, with 55 s holds. Table 1 details the operational conditions of each cycling test. The Ag-coated cathode GDEs were then imaged *via* SEM after testing, and the catalyst layer morphology was compared to that of a pristine silver-

https://doi.org/10.1021/acsaem.2c01308
ACS Appl. Energy Mater. XXXX, XXX, XXX−XXX

Table 1. Parameters Used for Each of the AST Cycling Tests in This Study[a]

test name	max potential (in V, "on")	min potential (in V, "off")	amplitude (V)	scan rate (mV/s)	duration of 90 cycles (hours)
AST 1	−3.00	0 V	3.00	250	3.35
AST 2	−2.00	0 V	2.00	250	3.15
AST 3	−3.00	OCV	∼3.00	250	3.25
AST 4	−2.00	OCV	∼2.00	250	3.10
AST 5	−3.00	−1.75	1.25	250	3.00

[a]Amplitude of **AST 3** and **AST 4** is denoted as approximate due to varying OCV throughout the test.

coated GDE. Additionally, GDE composition was analyzed *via* EDX, XRD, and GI-XRD.

2.4. Electrode Characterization Protocol. Before testing, fresh electrodes were imaged using SEM (FEI Quanta FEG 450 ESEM); the microscope was operated at 15 kV, and images were taken at 80×, 250×, 500×, 1000×, and 5000× magnification in order to compare overall surface morphology as well as microscale structure after operation in various conditions. Approximately 70% of the exposed electrode surface was imaged at a low magnification. EDX (FEI Quanta FEG 450 ESEM) was performed using the same instrument; each sample was scanned across a surface area of 0.5 and 0.04 mm^2 to compare the presence of carbon, fluorine, silver, and potassium (from the electrolyte) at various length scales. The sample composition was additionally analyzed using XRD (PANalytical Philips X'pert MRD System #2); the source was operated at 45 kV and 40 mA current. 30 min scans of each sample were taken; the 2θ angle was swept from 5 to 100°. XRD peaks were analyzed using Jade software, and peaks were matched with the powder diffraction database from the International Center for Diffraction Data. Post-testing, electrodes

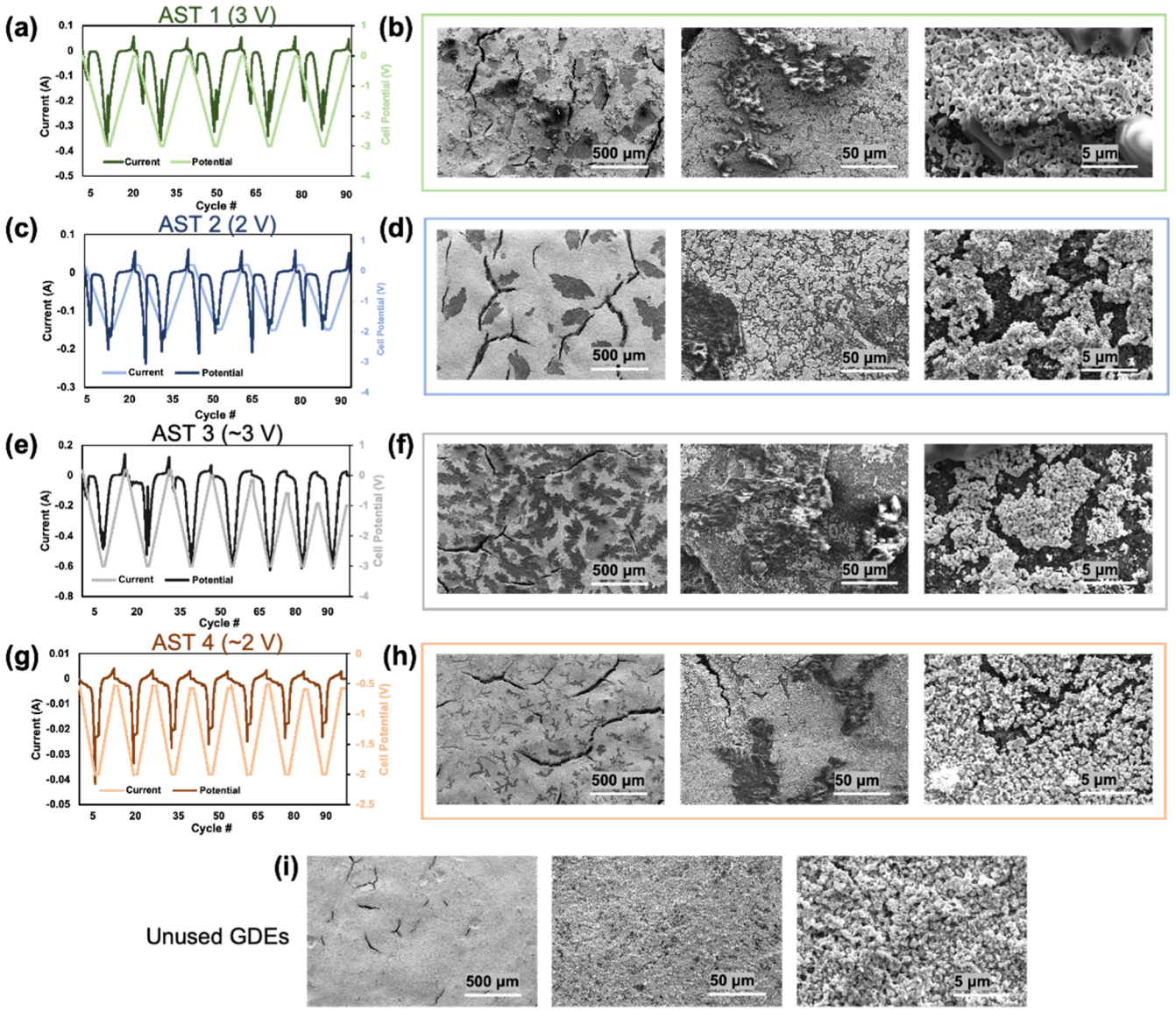

Figure 1. (a) Periodic cycles from **AST 1** with the applied potential in light blue and the current response in dark blue; (b) SEM images of the cathode after **AST 1** taken at 100×, 1000×, and 10,000× magnification; (c) periodic cycles from **AST 2**; (d) SEM images of the cathode after **AST 2** taken at 100×, 1000×, and 10,000× magnification; (e) periodic cycles from **AST 3**; (f) SEM images of the cathode after **AST 3** taken at 100×, 1000×, and 10,000× magnification; (g) periodic cycles from **AST 4**, along with an inset of the OCV taken after each 20 cycles; (h) SEM images of the cathode after **AST 1** taken at 100×, 1000×, and 10,000× magnification; and (i) SEM images of a pristine GDE taken at 100×, 1000×, and 10,000× magnification for comparison to post-testing cathode images.

https://doi.org/10.1021/acsaem.2c01308
ACS Appl. Energy Mater. XXXX, XXX, XXX−XXX

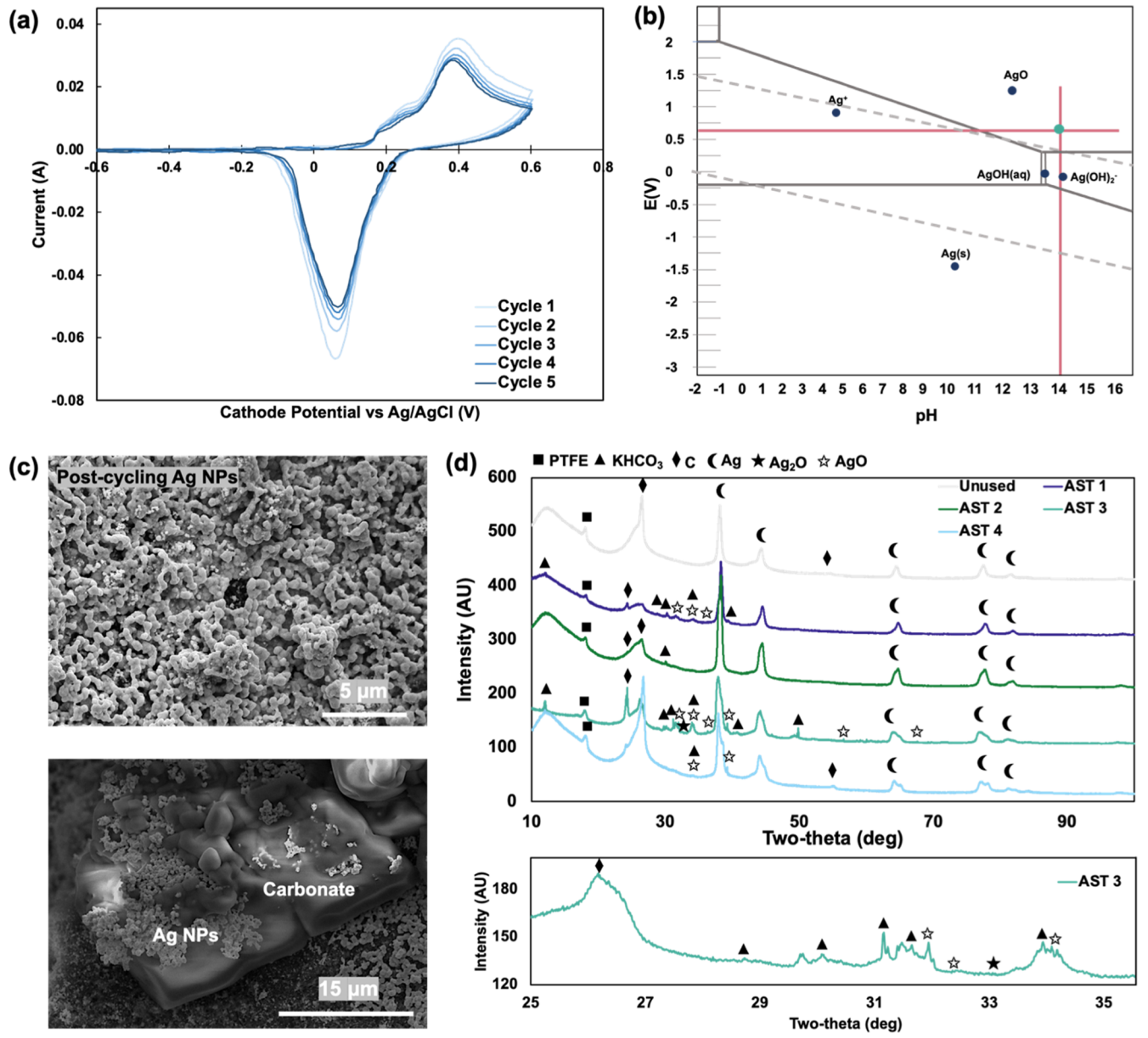

Figure 2. (a) Five CVs performed on pristine blank silver GDE in 2 M KOH—cathode potential was swept from −1.5 to 0.6 V *vs* Ag/AgCl; (b) Ag Pourbaix diagram (created with data from open sources);[23,24] (c) SEM images of the cathode used in **AST 3** showing the presence of small particles among the larger Ag nanoparticles and on top of carbonate deposits formed during operation, supporting our hypothesis that these particles were redeposited on the surface during each reduction sweep of the potential cycle; (d) GIXRD peaks for unused GDE and cathodes from **AST 1**−**4**, identifying key surface species. Inset for **AST 3** provided to show more detail of oxide peaks.

were rinsed with DI water and dried with N_2; all of the above measurements (SEM, EDX, and XRD) were repeated on the used electrodes.

3. RESULTS AND DISCUSSION

3.1. GDE Degradation *via* Oxide Formation. Figure 1 presents the electrochemical response and post-testing SEM images for the cathodes used in **AST 1**−**4**. The potential−current graphs are color coded and are labeled with the test name (**AST X**) and amplitude of applied potential. Figure 1a shows the applied potential waveform and current response for **AST 1**, sampled once every 15 cycles for visual clarity. Notably, there are three peaks present per cycle; a small oxidation wave, a subsequent reduction wave, and a following larger reduction wave at CO_2 reduction potentials. An inset presenting one cycle in greater detail for each test can be found in Figure S1. In Figure 1b, SEM images at low (100×), medium (1000×), and high (10,000×) magnification of the surface of the cathode post-testing are presented. In this test, carbonate deposits formed as large crystals on the GDE surface, similar in morphology to those seen in our previous work and identified as $KHCO_3$.[16,17] Since the average current density for **AST 1** during the holds at −3 V was −320 mA cm^{-2}, this carbonate formation is consistent with previous work, which showed widespread carbonate formation at −200 mA cm^{-2} in 2 M KOH.[16] Significant cracking and removal of areas of the catalyst layer can be seen, as well as morphology change of Ag catalyst nanoparticles visible in the high magnification images. Similarly, Figure 1c presents the potential and current response for **AST 2**, and Figure 1d presents SEM images of the surface.

https://doi.org/10.1021/acsaem.2c01308
ACS Appl. Energy Mater. XXXX, XXX, XXX−XXX

The figure shows the presence of deformation and removal of some sections of Ag catalysts, leaving patches of bare carbon GDE substrate below. Some carbonate deposits are also present but are less widespread at high magnification; this is expected due to the lower average current density during the −2 V holds (−12 mA cm^{-2}).

Figure 1e shows the applied potential and response for **AST 3**. The evolution of the OCV over the duration of the test is presented in Figure S1; notably, the OCV evolves gradually from an initial value of 0.173 V to a more negative −0.665 V by the end of the 90 cycles. Figure 1f shows the surface of the GDE after testing, where again we can see both carbonate deposits and cracking/removal of the catalyst layer, as well as catalyst morphology change at high magnification. Figure 1g presents current response and OCV data for **AST 4**, and Figure S1 shows that after the first OCV measurement of 0.268 V, the subsequent measurement is −0.535 V, and the OCV is consistent around this value for the remainder of the cycles. This difference may be due to the lower applied potential and average current density during this test. Figure 1h shows the surface of the cathode after **AST 4**. Notably, when comparing Figure 1f,h, we can more clearly compare the extent of the carbonate deposits in the low magnification images. In prior work, we showed the increasing rate of deposit formation with increased applied current/cell potential, so we expected more deposit formation in **AST 1** and **AST 3**, which had a high maximum applied potential of −3 V.[15] Both cathodes from **AST 3** and **AST 4** have some carbonate deposits present on the surface and show significant cracking and restructuring of the catalyst layer. Figure 1i shows the surface of an untested cathode for comparison to the other SEM images; at high magnification, the normal morphology of the Ag nanoparticle catalyst is shown. Based on these results, we identified a novel degradation mechanism indicated by the restructuring and removal of the Ag catalyst layer during potential cycling. We hypothesized that this catalyst layer restructuring was related to the presence of the oxidation and reduction peaks observed when cycling to more positive potentials. EDX maps of the surface give more insight into the catalyst layer degradation and can be found in Figure S2.

To further explore the degradation of the catalyst layer observed in these cycling tests, we performed cyclic voltammetry (CV), controlling cathode potential on fresh Ag-coated cathodes. The resulting CVs can be seen in Figure 2a. Two small oxidation waves occurred at 180 and 260 mV *versus* Ag/AgCl (−110 and 150 mV cell potential), a large oxidation wave occurred at 415 mV *versus* Ag/AgCl (0 V cell potential), and a reduction wave occurred at 23.5 mV *versus* Ag/AgCl (−283 mV cell potential). The height of both the oxidation and reduction peaks decreased over five CV cycles. Previous literature details the formation of silver oxides on silver electrodes in alkaline media, showing multiple oxide and reduction peaks which closely correspond to our potential range of interest.[18−21] We determined *via* Ag Pourbaix diagrams (Figure 2b) that the presence of silver oxides was thermodynamically possible under our operating conditions.[19] We used the following equations from Sato and Shimizu to describe the oxidation reactions, leading first to the formation of Ag_2O and then the subsequent formation of AgO.[20] These equations show that the formation of Ag_2O (eq 1) occurs around 145 mV *versus* Ag/AgCl, and then, the subsequent formation of AgO (eq 2) occurs around 410 mV *versus* Ag/AgCl.[22]

$$2Ag^+ + 2OH^- \rightleftharpoons Ag_2O + H_2O + 2e^- \quad (0.342\ \text{V vs SHE},\ 0.145\ \text{V vs Ag/AgCl}) \tag{1}$$

$$Ag_2O + 2OH^- \rightleftharpoons 2AgO + H_2O + 2e^- \quad (0.607\ \text{V vs SHE},\ 0.410\ \text{V vs Ag/AgCl}) \tag{2}$$

Additional small peaks present in the oxidative sweep are attributed to adsorption processes, the formation of an oxide monolayer, and dissolution processes.[19] In contrast to previous work, we see a single reduction peak rather than multiple reduction peaks for the silver oxides formed in the catalyst layer. Work by Wan *et al.* shows post-oxidation SEM images of Ag_2O crystals, ranging in size from 100−250 nm, matching the morphology of the catalyst shown in our post-testing high-magnification SEM images.[21] From this evidence, we conclude that during the positive potential sweep, Ag_2O and AgO are formed in the catalyst layer and then subsequently reduced during the negative potential sweep. Dissolution of silver oxides is also noted under alkaline conditions, resulting from either the formation of $Ag(OH)_2^-$ or natural slight solubility of AgO (1.7×10^{-4} M/L).[19,20] In our system, degradation and removal of the catalyst layer occur under these conditions as some of the oxidized silver is dissolved and swept out of the cell with the flowing electrolyte, while the rest is redeposited on the catalyst layer surface during the reduction sweep. Additional SEM images of the cathode used in **AST 3**, presented in Figure 2c, show small silver particles (average radius 0.2 μm *vs* 1 μm for the pristine Ag nanoparticles) on the catalyst layer surface and on top of carbonate crystals, indicating their deposition after being dissolved in solution during cycling. Each of these **AST 1−4** protocol experiments were repeated. SEM images of cathodes used in these repeats of the **AST 1−4** protocols revealed similar cracking and loss of the silver catalyst layer. SEM images of the surfaces of cathodes tested in both trials of **AST 1** can be found in Figure S3.

Additionally, more information is provided in Figure 2d, which shows grazing-incidence XRD (GIXRD) measurements carried out on the cathodes from **AST 1−4**. All four cathodes show the presence of $KHCO_3$, confirming the identity of the carbonate deposits, but making the identification of oxides difficult as there is significant overlap between peaks belonging to $KHCO_3$ and Ag_2O_2. However, peaks belonging to AgO can been seen around 32, 34, and 36°, especially in the cathode used in **AST 3**, which is shown in more detail in the inset of Figure 2d. This result strengthens our hypothesis that the formation of oxide, along with dissolution and subsequent removal in the electrolyte stream, causes widespread loss and removal of the catalyst layer, resulting in loss of CO_2 to CO conversion by the system after only 15 cycles (Figure S4).

We propose that the formation of Ag oxides and subsequent loss of the catalyst through dissolution and catalyst layer restructuring explain the degradation of our Ag-nanoparticle cathode layer when our system is operated in the relevant oxide formation potential range. Through successive cycles of oxidation and reduction, the catalyst layer is restructured, and catalyst material is lost, halting conversion of CO_2 to CO. We identify this oxide formation potential range as beginning at potentials more positive than 180 mV cathode potential *versus* Ag/AgCl (−110 mV cell potential) in our alkaline flow system. Similar CO_2RR systems using Ag-based cathodes and cycling through startup and shutdown should apply a consistent

https://doi.org/10.1021/acsaem.2c01308
ACS Appl. Energy Mater. XXXX, XXX, XXX−XXX

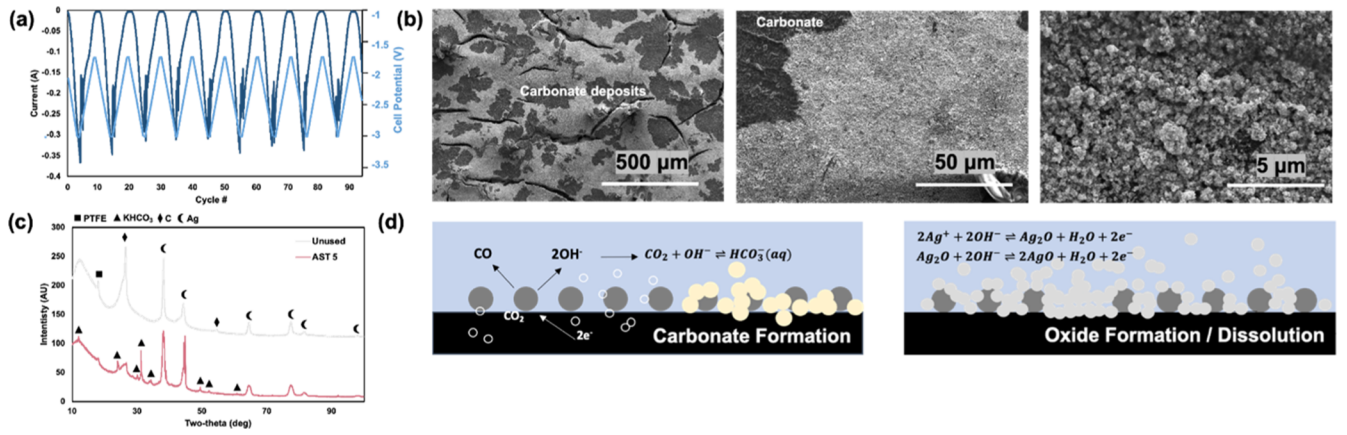

Figure 3. (a) Current response for **AST 5**; (b) SEM images of the cathode used in **AST 5** taken at 100×, 1000×, and 10,000× magnification; (c) GIXRD for an unused Ag-coated GDE and the cathode used in **AST 5**, showing the presence of potassium bicarbonate on the surface; and (d) comparison of degradation mechanisms found at low potential (carbonate formation) and high potential (oxide formation and dissolution).

Table 2. Parameters Used for Each of the Carbonate Inhibition Cycling Tests Employed; These Values are the Applied Testing Conditions and Not Measured Results[a]

test name	maximum potential (V)	minimum potential (V)	operational time (seconds)	recovery time (seconds)	total duration (hours)
inhibition 1	−2.75	−1.60	60	30	6
inhibition 2	−2.75	−1.60	30	15	6
inhibition 3*	−2.75	−1.60	60	30	6
inhibition 4*	−2.75	−1.60	30	15	6
control 1	−2.75	−1.60	N/A	N/A	4
control 2*	−2.75	−1.60	N/A	N/A	4

[a]Tests marked with a * were repeat trials confirming the degree of carbonate formation on GDEs under the chosen operating conditions.

negative counter potential to avoid this oxide formation range or will risk significant degradation of the catalyst layer *via* oxide formation and dissolution.

3.2. GDE Degradation *via* Carbonate Formation at Low Potentials. Figure 3 reports the results of **AST 5**, which was chosen as a control to compare previous results from **AST 1−4** with cycling at the same scan rate between potentials in the CO_2 formation range. Since the onset of CO_2 reduction is seen at −1.6 V cell potential in our system, the system was cycled at operating potentials more negative than this onset to determine the impact of cycling within the CO_2 reduction range on the cathode. The current response pictured in Figure 3a shows that there is one large reduction peak per cycle, corresponding with CO_2 reduction as expected. Noise in the current response is due to the formation of gas product bubbles at the cathode at high current densities.[25] Post-testing SEM in Figure 3b shows widespread carbonate formation on the surface of the GDE, but no cracking and loss of the catalyst layer or nanoparticle morphology change. Figure 3c shows GI XRD peaks for an unused cathode and the cathode used in **AST 5**, identifying the presence of $KHCO_3$ on the used cathode surface but not any additional silver oxides. Thus, we hypothesize that carbonate formation, not Ag-oxide formation and dissolution, is the major cause of the performance loss if the system is cycled at negative potentials within the CO_2 reduction range (Figure 3d). This hypothesis aligns with results from our recent work on carbonate deposit formation as a major degradation mechanism in alkaline flow systems.[16] EDX mapping of the surface of the cathode used in **AST 5** can be found in Figure S2.

3.3. GDE Stability Enhancement *via* Carbonate Inhibition Cycling. Next, employing strategies from our **AST** cycling tests, we wanted to explore the potential for the tailored application of potential cycling to improve GDE durability. We showed in our previous work that carbonate deposit formation on the cathode is dependent on operating current density and potential of our system, specifically noting that at higher currents/potentials, deposit formation is more widespread.[16] We hypothesized there that the formation of carbonates at the reaction interface was being driven by OH^- production from the reduction of CO_2 to CO and OH^-, resulting in a high concentration of $KHCO_3$ which then exceeds solubility limits locally, precipitating and forming deposits on the cathode surface. Thus, carbonate formation is influenced not only by the electrolyte composition and concentration but also by the activity of the cathode, controlled by either applied current or potential. In control experiments where our system was operated with flowing 3 M KOH and CO_2, we did not see carbonate deposit formation on the cathode surface, reinforcing the key role of applied current/potential in the formation of these deposits.[16] From this information, we hypothesized that a potential cycling method could be used to inhibit the nucleation and growth of carbonate deposits on the cathode surface. A recent paper from Xu *et al.* showed extremely promising results with a potential cycling method in their GDE-based MEA system; previously, they had seen carbonate deposit formation on their cathode after 10 h but were able to operate the system for 157 h by cycling the cell potential from an operational potential of −4 V to a recovery potential of −2 V.[26] However, this method has not been attempted in a flow system, where carbonate deposit formation is extremely rapid due to the aqueous alkaline catholyte which is in constant contact with the cathode. Therefore, we decided to attempt a proof-of-concept cycling

https://doi.org/10.1021/acsaem.2c01308
ACS Appl. Energy Mater. XXXX, XXX, XXX−XXX

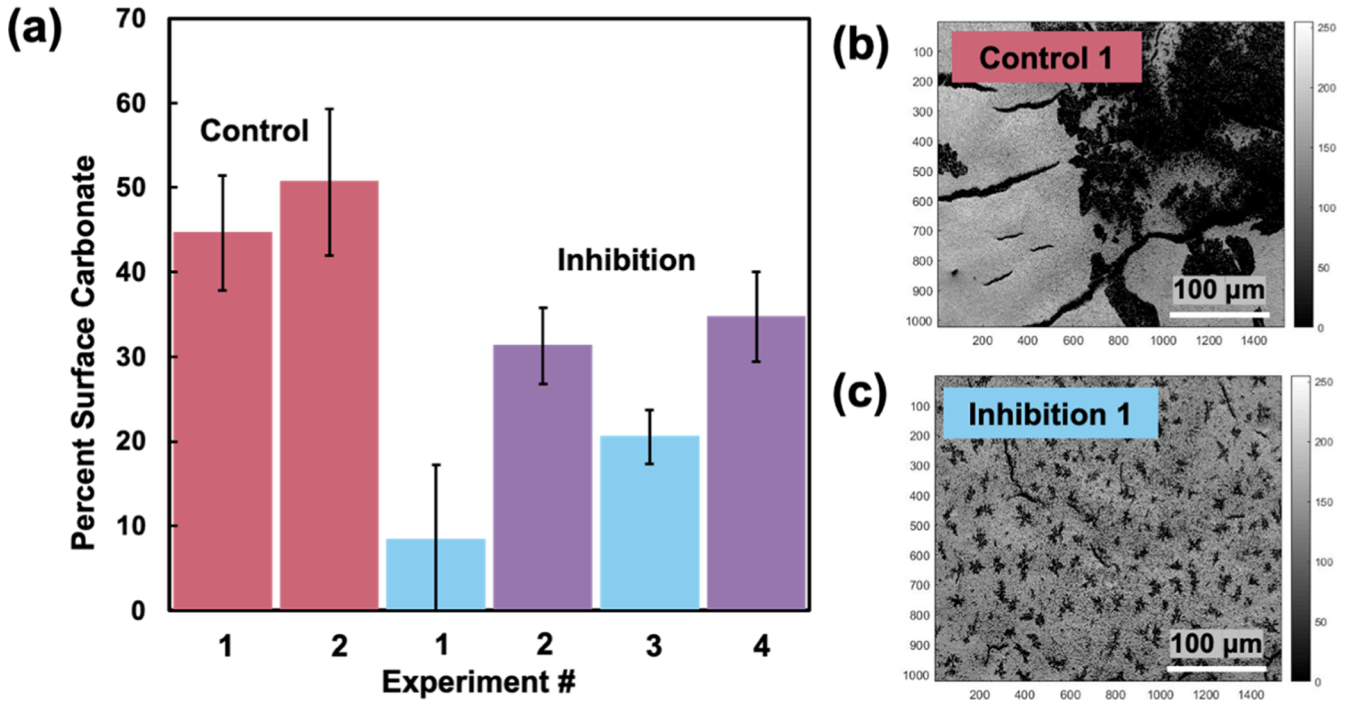

Figure 4. (a) Percent surface carbonate for control *vs* cycling inhibition experiments; experiments that repeated the same conditions have the same colored bars, red for control experiments, blue for Inhibitions 1 and 3 (60 s at −2.75 V/30 s at −1.6 V), and purple for Inhibitions 2 and 4 (30 s at −2.75 V/15 s at −1.6 V); (b) SEM image of the used cathode from control; and (c) SEM image of the used cathode from the cycling test, showing fewer surface carbonate deposits.

method for carbonate deposit inhibition in our alkaline flow system.

In order to avoid the formation of silver oxide, we chose a recovery potential of −1.60 V, well below the oxide formation region but above the onset potential of CO_2 reduction. According to Xu *et al.*, this recovery potential is essential to disrupt the production of hydroxide ions at the reaction interface during the recovery period. By cycling between operational and recovery potential, the carbonate ions can migrate to the anode during recovery periods, preventing precipitation and deposit formation at the cathode. We alternated trials applying two different potential waveforms to our system, controlling the whole cell potential; a step function where the potential was alternated between 60 s at −2.75 V and 30 s at −1.60 V (Inhibition 1 and 3) and a step function where the potential was alternated between 30 s at −2.75 V and 15 s at −1.60 V (Inhibition 2 and 4). Both methods were applied for 6 h to our system while using a 2 M KOH electrolyte and are described in Table 2.

Control experiments were also performed where a constant −2.75 V cell potential was applied to the system for 4 h, corresponding to the total duration that this operational potential was applied in Inhibition 1 and 3 tests since one-third of the total testing time was spent in the recovery potential for each test. As shown in Figure 4a, the percent surface carbonate of used GDEs was calculated using MATLAB image analysis of post-testing SEM images. When surface coverage of carbonate deposits was compared between the cycling and control experiments, we saw a reduction of 51% of carbonate deposits on the catalyst layer between the average control method and average cycling method. More information on the surface carbonate coverage comparison and image analysis can be found in Figures S5 and S6. Inhibition methods 1 and 3 that used a 30 s recovery periods appear to have been slightly more successful at inhibiting carbonate formation, with an average post-testing carbonate surface coverage of 15% *versus* 33% for Inhibition methods 2 and 4 that used a 15 s recovery period. This is likely due to the beneficial effects of a longer period, in which the flowing electrolyte could be refreshed at the catalyst layer.

Figure 4b shows the surface of the Ag-coated cathode, imaged *via* SEM after a control experiment constant cell potential application (−2.75 V), and Figure 4c shows the surface of another cathode after cycling (60 s at −2.75 V/30 s at −1.60 V). In both experiments, the currents during the application of −2.75 V were around −200 mA cm^{-2}. In the control experiment, formation of large regions of carbonate (dark patches) is visible on the surface, while in the cycling experiment, carbonates adhered to the surface are smaller and more dispersed, covering less catalyst layer surface area. The presence of smaller, dispersed carbonates rather than large regions of concentrated deposits indicates that deposit growth was halted during the application of the recover potential, resulting in more nucleation sites of the deposits rather than continuous growth of existing deposits. Additional SEM images of these dispersed carbonates on the surface can be seen in Figure S4.

Potential cycling shows promise for the interruption of carbonate deposition *via* periodically lowering OH^- concentration at the catalyst surface, thus interrupting formation of $KHCO_3$. As this work was intended to serve as a proof of concept, future work should focus on the optimized duration and potential of recovery periods in order to reach the goal of eliminating carbonate deposits. Complete elimination of deposits may be difficult in a flow electrolyzer with an alkaline liquid catholyte, but this method can be further explored in MEA using humidified CO_2 at the cathode. Additionally, impact of potential cycling on product formation should be

https://doi.org/10.1021/acsaem.2c01308
ACS Appl. Energy Mater. XXXX, XXX, XXX−XXX

quantified and analyzed for economic feasibility of potential cycling operational methods by future researchers to determine if this method is suitable for commercial operation of CO_2RR systems.

4. CONCLUSIONS

In this work, we explored the impact of variable potential cycling methods on durability and performance of Ag-coated GDEs for the conversion of CO_2 to CO in an alkaline flow electrolyzer. We sought to explore how cycling, both within the CO_2 reduction range and to OCV, the system's off state, would impact cathode performance and durability. To study these impacts on a laboratory time scale, we employed multiple **AST** protocols to simulate the impact of potential cycling on GDE durability and performance. To the best of our knowledge, this was the first study of its kind on Ag cathodes for CO_2RR. The results show that cycling to OCV causes significant degradation *via* the formation, reduction, and dissolution of Ag oxides in the catalyst layer. Notably, if exposed to cathode potentials above 0.180 V *versus* Ag/AgCl at the cathode, silver oxide formation will rapidly degrade the catalyst layer, changing the morphology of the layer and leading to loss of catalyst *via* dissolution. Thus, if CO_2RR systems are exposed to multiple cycles of startup and shutdown, care should be taken to implement a small continuous negative potential to avoid these oxide-forming potentials. Potential fluctuations at cathode potentials more negative than 0.180 V *versus* Ag/AgCl will not expose the GDE to degradation *via* silver oxide formation. In general, researchers wishing to carry out cycling-based accelerated durability testing should choose a potential range reflecting the operational potentials required to achieve high current densities in their systems; the potentials used in this work were specific to our flow electrolyzer/GDE-based system. This work provides insights into degradation caused by cycling into the oxide formation range and outlines the optimal cycling conditions for our system and similar Ag-coated GDEs. Carbonate formation on the GDE, however, is ubiquitous when operating in alkaline media at high current densities, an issue that must be addressed separately through different cell designs, over layers, or other approaches.

We also explored a strategy for carbonate inhibition consisting of applying repeated cycles of a negative operational potential and a less negative regeneration potential, as previously explored by other researchers in an MEA-based CO_2RR system. We found that applying 30 s of a regeneration potential of −1.60 V after 60 s of operation at −2.75 V successfully decreases carbonate deposit formation in 2 M KOH in our system over 6 h of cycling operation. When compared to constant applied potential experiments, we saw a 51% reduction in surface carbonate deposits on the catalyst layer. This strategy shows promise to prevent carbonate formation in a flow electrolyzer operated either continually or intermittently under alkaline conditions. Future work can determine the ideal parameters for cycling, which should be tailored to individual CO_2RR systems and cathodes, as well as depending on the desired operational potential. When looking at the big picture, additional strategies for carbonate inhibition in high-throughput systems using GDEs will be needed. These can include the implementation of MEA-based systems, which use humidified CO_2 instead of a liquid catholyte, thus leading to slower formation of deposits, as well as engineering the composition of the catholyte to inhibit the deposit formation and growth. Additionally, recent papers have shown promise in the direct conversion of CO_2 from liquid $KHCO_3$, eliminating loss of reactants to carbonate formation.[27]

Overall, we see that if alkaline CO_2RR systems employing silver catalysts are used at potentials near OCV, which might occur when systems are coupled with solar panels or other variable renewable power sources, oxide formation must be taken into consideration. Tailoring the applied potential and using cycling methodologies can be a useful tool for extending the durability of the system. By avoiding oxide formation and exploring further strategies for the mitigation of surface carbonate deposits, robust GDEs and CO_2RR electrolyzers can be implemented for the storage of excess renewable energy through the production of green chemicals and fuels.

■ ASSOCIATED CONTENT

Supporting Information

The Supporting Information is available free of charge at https://pubs.acs.org/doi/10.1021/acsaem.2c01308.

GIXRD penetration depth calculation, FE calculation, single cycle details and OCP measurements, EDX surface mapping, FE measurements for **AST 1**, post-testing SEM images, and MATLAB image analysis methodology (PDF)

■ AUTHOR INFORMATION

Corresponding Author

Paul J. A. Kenis − *Department of Chemical and Biomolecular Engineering, University of Illinois Urbana Champaign, Urbana 61801 Illinois, United States;* orcid.org/0000-0001-7348-0381; Email: kenis@illinois.edu

Authors

Emiliana R. Cofell − *Department of Materials Science and Engineering, University of Illinois Urbana Champaign, Urbana 61801 Illinois, United States*

Zachary Park − *Department of Chemical and Biomolecular Engineering, University of Illinois Urbana Champaign, Urbana 61801 Illinois, United States*

Uzoma O. Nwabara − *Department of Chemical and Biomolecular Engineering, University of Illinois Urbana Champaign, Urbana 61801 Illinois, United States*

Lauren C. Harris − *Department of Chemistry, University of Illinois Urbana Champaign, Urbana 61801 Illinois, United States*

Saket S. Bhargava − *Department of Chemical and Biomolecular Engineering, University of Illinois Urbana Champaign, Urbana 61801 Illinois, United States*

Andrew A. Gewirth − *Department of Chemistry, University of Illinois Urbana Champaign, Urbana 61801 Illinois, United States;* orcid.org/0000-0003-4400-9907

Complete contact information is available at: https://pubs.acs.org/10.1021/acsaem.2c01308

Notes

The authors declare no competing financial interest.

■ ACKNOWLEDGMENTS

The authors gratefully acknowledge Shell's New Energies Research and Technology (NERT) program for providing funding for this work. We would also like to acknowledge NERT's Dense Energy Carriers (DEC) team for their valuable inputs and discussions during the course of this work. We

would also like to acknowledge the International Institute of Carbon Neutral Energy Research (WPI-I2CNER) sponsored by the Japanese Ministry for Education, Culture, Sports, Science and Technology and the SURGE Fellowship for the funding of EC. We would like to acknowledge A.A.G., Stephanie Chen, and Z.P. for their insightful feedback and assistance during this project. Characterization was carried out in the following facilities: Fredrick Seitz Materials Research Laboratory and in the Beckmann Institute for Advanced Science and Technology Imaging Technology Group, University of Illinois at Urbana-Champaign.

REFERENCES

(1) Masson-Delmotte, V.; Zhai, P.; Pirani, A.; Connors, S. L.; Péan, C.; Berger, S.; Caud, N.; Chen, Y.; Goldfarb, L.; Gomis, M. I.; Huang, M.; Leitzell, K.; Lonnoy, E.; Matthews, J. B. R.; Maycock, T. K.; Waterfield, T.; Yelekçi, O.; Yu, R.; Zhou, B. *IPCC, 2021: Climate Change 2021: The Physical Science Basis*; Cambridge University Press, 2021.

(2) Tway, C.; Allen, D.; Barteau, M.; Burkart, M.; Dunn, J.; Gaffney, A.; Gupta, R.; Hazari, N.; Kanan, M.; Kenis, P.; Klee, H.; Sant, G. Report of Consensus Study issued by the National Academies of Sciences, Engineering, and Medicine. *Gaseous Carbon Waste Streams Utilization: Status and Research Needs*; The National Academies Press: Washington, DC, 2019.

(3) Jhong, H. R.; Ma, S. C.; Kenis, P. J. A. Electrochemical conversion of CO_2 to useful chemicals: current status, remaining challenges, and future opportunities. *Curr. Opin. Chem. Eng.* **2013**, *2*, 191−199.

(4) Hori, Y. Electrochemical Co_2 Reduction on Metal Electrodes. *Modern Aspects of Electrochemistry*; Springer, 2008; Vol. *42*, pp 89−189.

(5) Zhao, G.; Huang, X.; Wang, X.; Wang, X. Progress in catalyst exploration for heterogeneous CO2 reduction and utilization: a critical review. *J. Mater. Chem. A* **2017**, *5*, 21625−21649.

(6) Verma, S.; Hamasaki, Y.; Kim, C.; Huang, W.; Lu, S.; Jhong, H.-R. M.; Gewirth, A. A.; Fujigaya, T.; Nakashima, N.; Kenis, P. J. A. Insights into the Low Overpotential Electroreduction of CO2 to CO on a Supported Gold Catalyst in an Alkaline Flow Electrolyzer. *ACS Energy Lett.* **2018**, *3*, 193−198.

(7) Zhao, S.; Jin, R.; Jin, R. Opportunities and challenges in CO2 reduction by gold- and silver-based electrocatalysts: from bulk metals to atomically precise nanoclusters. *ACS Energy Lett.* **2018**, *3*, 452−462.

(8) Endrődi, B.; Bencsik, G.; Darvas, F.; Jones, R.; Rajeshwar, K.; Janáky, C. Continuous-flow electroreduction of carbon dioxide. *Prog. Energy Combust. Sci.* **2017**, *62*, 133−154.

(9) Bhargava, S. S.; Proietto, F.; Azmoodeh, D.; Cofell, E. R.; Henckel, D. A.; Verma, S.; Brooks, C. J.; Gewirth, A. A.; Kenis, P. J. A. System Design Rules for Intensifying the Electrochemical Reduction of CO2 to CO on Ag Nanoparticles. *Chemelectrochem* **2020**, *7*, 2001−2011.

(10) Verma, S.; Kim, B.; Jhong, H.-R. M.; Ma, S.; Kenis, P. J. A. A Gross-Margin Model for Defining Technoeconomic Benchmarks in the Electroreduction of CO_2. *ChemSusChem* **2016**, *9*, 1972−1979.

(11) Jouny, M.; Luc, W.; Jiao, F. General Technoeconomic Analysis of CO2 Electrolysis Systems. *Ind. Eng. Chem. Res* **2018**, *57*, 2165−2177.

(12) Nwabara, U. O.; Cofell, E.; Verma, S.; Negro, E.; Kenis, P. J. A. Durable Cathodes and Electrolyzers for the Efficient Aqueous Electrochemical Reduction of CO_2. *ChemSusChem* **2020**, *13*, 855−875.

(13) Inman, R. H.; Pedro, H. T. C.; Coimbra, C. F. M. Solar forecasting methods for renewable energy integration. *Prog. Energy Combust. Sci.* **2013**, *39*, 535−576.

(14) Martín, A. J.; Larrazábal, G. O.; Pérez-Ramírez, J. Towards sustainable fuels and chemicals through the electrochemical reduction of CO2: lessons from water electrolysis. *Green Chem.* **2015**, *17*, 5114−5130.

(15) Zhang, S.; Yuan, X.-Z.; Wang, H.; Merida, W.; Zhu, H.; Shen, J.; Wu, S.; Zhang, J. A review of accelerated stress tests of MEA durability in PEM fuel cells. *Int. J. Hydrogen Energy* **2009**, *34*, 388−404.

(16) Cofell, E. R. N.; Nwabara, O.; Bhargava, S. S.; Henckel, D. E.; Kenis, P. J. A. Investigation of Electrolyte-Dependent Carbonate Formation on Gas Diffusion Electrodes for CO_2 Electrolysis. *ACS Appl. Mater. Interfaces* **2021**, *13*, 15132−15142.

(17) Bhargava, S. S.; Cofell, E. R.; Chumble, P.; Azmoodeh, D.; Someshwar, S.; Kenis, P. J. A. Exploring multivalent cations-based electrolytes for CO2 electroreduction. *Electrochim. Acta* **2021**, *394*, 139055.

(18) Jhong, H. R. M.; Brushett, F. R.; Kenis, P. J. A. The Effects of Catalyst Layer Deposition Methodology on Electrode Performance. *Adv. Energy Mater.* **2013**, *3*, 589−599.

(19) Droog, J. M. M.; Alderliesten, P. T.; Bootsma, G. A. Initial Stages of Anodic Oxidation of Silver in Sodium Hydroxide Solution Studied by Potential Sweep. *J. Electroanal. Chem.* **1979**, *99*, 173−186.

(20) Sato, N.; Shimizu, Y. Anodic Oxide on Silver in Alkaline Solution. *Electrochim. Acta* **1973**, *18*, 567−570.

(21) Wan, Y.; Wang, X.; Liu, S.; Li, Y.; Sun, H.; Wang, Q. Effect of Electrochemical Factors on Formation and Reduction of Silver Oxides. *Int. J. Electrochem. Sci.* **2013**, *8*, 12837−12850.

(22) Hur, T. U.; Chung, W. S. The Mechanism of Silver(I) Oxide to Silver(II) Oxide Formation on Polycrystalline Silver Electrodes in 8 M KOH Solution. *J. Electrochem. Soc.* **2005**, *152*, A996−A1000.

(23) Pourbaix Diagram: Ag. https://materialsproject.org/#apps/pourbaixdiagram/{%22chemsys%22%3A[%22Ag%22]} (accessed January 2022).

(24) Research Center for Deep Geological Environments. *Atlas of Eh-pH Diagrams-Intercomparison of Thermodynamic Databases Geological Survey of Japan Open File Report No.419*; National Institute of Advanced Industrial Science and TechnologyNaoto TAKENO, 2005.

(25) Lee, C.; Zhao, B.; Lee, J. K.; Fahy, K. F.; Krause, K.; Bazylak, A. Bubble Formation in the Electrolyte Triggers Voltage Instability in CO2 Electrolyzers. *iScience* **2020**, *23*, 101094.

(26) Xu, Y.; Edwards, J. P.; Liu, S.; Miao, R. K.; Huang, J. E.; Gabardo, C. M.; O'Brien, C. P.; Li, J.; Sargent, E. H.; Sinton, D. Self-Cleaning CO_2 Reduction Systems: Unsteady Electrochemical Forcing Enables Stability. *ACS Energy Lett.* **2021**, *6*, 809−815.

(27) Li, Y. C.; Lee, G.; Yuan, T.; Wang, Y.; Nam, D.-H.; Wang, Z.; García de Arquer, F. P.; Lum, Y.; Dinh, C. T.; Voznyy, O.; Sargent, E. H. CO_2 Electroreduction from Carbonate Electrolyte. *ACS Energy Lett.* **2019**, *4*, 1427−1431.

https://doi.org/10.1021/acsaem.2c01308
ACS Appl. Energy Mater. XXXX, XXX, XXX−XXX